Rapid pacing by circulating traveling waves improves maturation of hiPSC-derived cardiomyocytes in self-organized tissue ring

Junjun Li[1,2#], Lu Zhang[3#], Leqian Yu[2], Itsunari Minami[4], Marcel Hörning[2,9], Ji Dong[5], Jing Qiao[2], Nanae Fujimoto[1,2], Yuji Shiba[6], Yang Zhao[7], Fuchou Tang[5], Shigeru Miyagawa[1], Yong Chen[2, 8], Yoshiki Sawa[1]*, Chao Tang[3]* and Li Liu[1,2]*

[1] Department of Cardiovascular Surgery, Osaka University Graduate School of Medicine, 2-2 Yamadaoka, Suita, Osaka 565-0871, Japan

[2] Institutes for Integrated Cell-Material Sciences (WPI-iCeMS), Kyoto University, Yoshida-Ushinomiya-cho, Sakyo-ku, Kyoto 606-8501, Japan

[3] Center for Quantitative Biology and Peking-Tsinghua Center for Life Sciences, Academy for Advanced Interdisciplinary Studies, Peking University, Beijing 100871, China

[4] Department of Cell Design for Tissue Construction Faculty of Medicine, Osaka University, Osaka 565-0871, Japan

[5] Biomedical Pioneering Innovation Center, College of Life Sciences, Peking University, Beijing 100871, China

[6] Institute for Biomedical Sciences, Department of Regenerative Science and Medicine, Shinshu University, 3-1-1 Asahi, Matsumoto, Nagano 390-0821, Japan

[7] State Key Laboratory of Natural and Biomimetic Drugs, the MOE Key Laboratory of Cell Proliferation and Differentiation, Institute of Molecular Medicine, Peking-Tsinghua Center for Life Sciences, Peking University, Beijing 100871, China

[8] PASTEUR, Département de chimie, école normale supérieure, PSL Research University, Sorbonne Universités, UPMC Université Paris 06, CNRS, 75005, France

[9] Present address: Institute of Biomaterials and Biomolecular Systems, University of Stuttgart, 70569 Stuttgart, Germany

[#] These authors contributed equally to this work.

* Correspondence to: Li Liu (li-liu@surg1.med.osaka-u.ac.jp), Chao Tang (tangc@pku.edu.cn) and Yoshiki Sawa (sawa-p@surg1.med.osaka-u.ac.jp).

Abstract

Directed differentiation methods allow acquisition of high-purity cardiomyocytes (CMs) differentiated from human induced pluripotent stem cells (hiPSCs); however, their immaturity characteristic limits their application for drug screening and regenerative therapy. The rapid electrical pacing of cardiomyocytes have been used for efficiently promoting the maturation of cardiomyocytes, here we describe a simple device in modified culture plate on which hiPSC-derived CMs (hiPSC-CMs) can form three-dimensional self-organized tissue rings (SOTRs). Using calcium imaging, we show that within the ring, traveling waves (TWs) of action potential spontaneously originated and ran robustly at a frequency up to 4 Hz. After 2 weeks, SOTRs with TW training showed matured features including structural organization, increased cardiac-specific gene expression, enhanced Ca^{2+}-handling properties, an increased oxygen-consumption rate, and enhanced contractile force. We subsequently used a mathematical model to interpret the origination, propagation, and long-term behavior of the TWs within the SOTRs. This new idea for spontaneous hiPSC-CM maturation also has potential for pacing the electrical excitable cells such as neuron and retina cells for various applications.

Introduction

Although human induced pluripotent stem cell-derived cardiomyocytes (hiPSC-CMs) have been proposed as an abundant resource for tissue engineering, drug screening, and regenerative-medicine applications[1], they exhibit characteristics different from adult human CMs, including immature sarcomere structure and morphology, a fetus-like gene-expression profile, and inadequate Ca^{2+}-handling properties[2-4]. The immature nature of hiPSC-CMs

55 potentially hinders their reflection of adult heart physiology for disease modeling and drug

56 assessment.

57   To achieve higher degrees of CM maturation and function, a variety of methods have

58 been developed, including dynamic culture[5], three-dimensional (3D) engineered heart

59 tissue[6,7], 3D printing[8], addition of factors[9], extracellular matrix[9,10], and external stimulation.

60 Electrical stimulation, especially high-frequency pacing, has long been suggested as an

61 effective method for maturing muscle cells[11-14], which upregulates cardiac markers[12,13,15],

62 enhances Ca^{2+}-handling properties[3], and promotes CM alignment[16]. During this process,

63 appropriate stimulation protocols are required to minimize possible tissue damage[17].

64 Additionally, it remains challenging to rapidly pace CM tissues (≥ 2 Hz) over long time[18] due

65 to possible side effects, such as heavy metal poisoning, electrolysis, pH shift, and the

66 generation of reactive oxygen species (ROS)[19,20]. Moreover, upscaling for mass stimulation is

67 either difficult or requires high level of power consumption[18]. As an important complement,

68 mechanical stimulation can promote CM maturation, with cyclic mechanical stress applied by

69 external stretching devices capable of forcing muscle-cell assembly into structurally and

70 functionally aligned 3D syncytium[21], thereby affecting their gene expression[22-24] and Ca^{2+}

71 cycling[25].

72   On another hand, spiral waves (traveling waves) within cardiac tissue have long been

73 investigated as a model for arrhythmia studies[26-29], and the rapid beating caused by in-vivo

74 spiral wave could lead to dysfunction of heart and even death of a patient. However, when

75 used in in-vitro condition, the rapid pacing by spiral wave, similar to rapid electrical

76 stimulation, could be beneficial for cardiomyocytes maturation.

77   In this study, we created a platform capable of promoting rapid formation of hiPSC-

78 CMs into 3D self-organized tissue rings (SOTRs), where propagation of an action potential in

79 the form of traveling waves (TWs) can spontaneously originate and travel around the close-

80   looped circuit, thereby making the CMs beat at a high frequency (~2–4 Hz) continuously and

81   robustly up to more than 89 days without any external stimulation. Additionally, we found

82   that the beating frequency and the TW speed could be adjusted by changing the diameter of

83   the ring. Furthermore, we constructed a mathematical model in order to elucidate the

84   origination, propagation, and long-term behavior of the TWs, with the model ultimately

85   agreeing well with the experimental data. After 2 weeks of training using the TWs, the

86   SOTRs demonstrated improved structural organization, upregulated cardiac-specific gene

87   expression, enhanced Ca^{2+}-handling properties, an increased oxygen-consumption rate (OCR),

88   and enhanced contractile force.

89   Although the maturation level of CMs trained with TWs remains lower than that

90   acquired using state-of-art methods[13], the maturation process demonstrated in the present

91   study was spontaneous and required no elaborate experimental setup and/or external

92   stimulation. Moreover, the mass production of matured CMs would be possible by simply

93   modifying conventional Petri dishes. Our results demonstrated a novel approach for

94   promoting spontaneous CM maturation and could serve as an economical and practical

95   system for future production of matured hiPSC-CMs.

96

Results

Self-organization of a hiPSC-CM ring

99   We created 3D SOTRs by plating hiPSC-CMs in a culture dish with a pillar in the center,

100   around which the CMs aggregated and formed a thick tissue ring within 2 days (Fig. 1a–c and

101   Supplementary Fig. 1). As indicated by the genetically encoded calcium indicator GCaMP,

102   we found looped activation propagations within the SOTRs (i.e., TWs; Supplementary Video

103   1), with from zero to three TWs present in one SOTR (Fig. 1d and e; and Supplementary

104   Video 2).

4

105   A trace recording (Fig. 1d and e) indicated no long rest periods between successive

106   TWs, resulting in higher beating rates in SOTRs capable of sustaining a higher number of

107   TWs (Fig. 1e and f). The spontaneous beating rate of SOTRs with zero TWs was 0.21 ± 0.10

108   Hz on day 6 and remained stable for 2 weeks, whereas the rates of SOTRs with one or two

109   TWs on day 6 were much higher (2.40 ± 0.49 Hz and 3.30 ± 0.39 Hz, respectively). Notably,

110   the wave speed in the TW groups was much lower (~2 cm/s) than that of the spontaneous

111   beating group (0 TW; ~9 cm/s). It is possible that the slower speed together with the

112   shortened pacing interval and refractory period might be caused by the higher beating

113   frequency in the TW groups relative to that in the zero TW group (Supplementary Fig. 2),

114   which agrees with previous reports associated with excitable media[30-34].

115   The beating rates of the one and two TW groups increased slightly over 2 weeks of

116   culturing, reaching 3.03 ± 0.68 Hz and 3.92 ± 0.69 Hz on day 14, respectively. After a 6-day

117   culture, 83.8% of 204 SOTRs had one or two TWs, 14.2% had zero TWs, and 2% had three

118   TWs; however, these percentages changed after a 2-week culture to 28.5% with zero TWs,

119   48.9% with one TW, 22.6% with two TWs, and no SOTRs with three TWs (Fig. 2d). Noise

120   and disturbances, such as those during medium changing, might have provoked changes in

121   and/or disappearance of TWs. In the long-term culture, we found that TWs could be

122   maintained in SOTRs for >89 days (Supplementary Fig. 3).

123   To better understand the nature of these TWs according to their organization,

124   propagation, and long-time behavior, we constructed a mathematical model (Supplementary

125   Information and Supplementary Fig. 4) comprising a ring of cells, each of which can beat

126   spontaneously with an intrinsic frequency. The total number of the cells in each ring in the

127   model is proportional to the diameter of the ring. The coupling between neighboring cells

128   through gap junctions[35,36] gradually increases with time in order to simulate the self-

129   organization and formation processes of the SOTR. Initially, all cells were independently set

130   to a random phase of beating, with all cells beating independently. As the gap junctions form

131   and strengthen, the beating of one cell harbors an increasing probability of triggering beating

132   in its neighboring cell, thereby forming a propagating wave. Initially, these waves are

133   unsynchronized and short-lived, as they initiate, disappear, and sometimes meet and collide

134   (Supplementary Video 3). Over time, a SOTR is left with one dominant propagating-wave

135   mode comprising zero or more TWs (Fig. 2a and Supplementary Video 3), with this process

136   similar to that observed in our experimental findings (Supplementary Video 4). Notably,

137   SOTRs with one or two TWs accounted for most of the simulation samples, a trend also

138   observed in our experimental results (Fig. 2b).

139   We then investigated how TW features and properties were affected by characteristics,

140   such as ring diameter, in the mathematical model and experiments. The beating frequency of

141   cells in SOTRs decreased with increasing ring diameter, as shown with one TW in Fig. 2c.

142   We noted that a constant TW speed implied a linear decrease in beating frequency with ring

143   diameter (which is proportional to the ring perimeter), and that the greater the perimeter, the

144   more time the wave would spend to travel around it. However, the data in Fig. 2c show a

145   slower-than-linear decrease; therefore, we measured the wave speed, finding that it increased

146   along with ring diameter in both the simulation and experiment (Fig. 2d). As discussed in the

147   Supplementary Information, this was due to the ability of a single hiPSC-CM to

148   spontaneously beat. Cells in larger rings would wait longer for the next TW to arrive, thereby

149   making them easier to be activated by the wave front and resulting in a faster wave speed.

150   This insight allowed us to predict the speed of two and three TWs. As shown in Fig. 2e, the

151   prediction agreed well with our experimental results. Additionally, the mathematical model

152   showed that the maximum number of TWs that a SOTR could sustain increased along with

153   ring diameter, which was confirmed experimentally (Fig. 2f). Here, the mathematical model

154   predicted that SOTRs with a diameter of 17 mm could contain as many as 19 TWs.

6

155   Experimentally, we found that SOTRs with a 3-mm pillar were optimal based on their highest

156   occurrence of TWs (~90% at ≥1 TW) (Supplementary Fig. 5). Moreover, the beating

157   frequency of one TW was only slightly slower than that in SOTRs with a 1-mm pillar;

158   therefore, SOTRs with a 3-mm pillar were chosen for subsequent investigations.

159

160   **TWs promote genetic and structural maturation of hiPSC-CMs**

161   The human fetal heart rate varies, although it generally stabilizes at ~3 Hz, whereas the adult

162   human heart rate is ~1 Hz[37]. Electrical stimulation has been used to mature CMs by pacing

163   their beating at a certain higher-than-normal frequency relative to a normal human rate[3];

164   however, continuous and high electrical stimulation can cause cell damage. Here, TWs within

165   the SOTRs were able to make the CMs beat at various frequencies in the absence of external

166   stimulation.

167   We used RNA sequencing to compare gene-expression profiles among different

168   groups. Principal component analysis (PCA; Fig. 3a) and hierarchical clustering of Spearman

169   correlation results (Fig. 3b) showed closer correlations between hiPSC-CMs receiving

170   training by TWs as compared with those without TW training. Additionally, we found

171   different gene-expression patterns among zero, one, and two TW groups (Fig. 3c). Functional

172   annotation according to Gene Ontology (GO) analysis revealed that upregulated genes

173   (adjusted $P < 0.05$; fold change > 1.5) in SOTRs with two TWs relative to those with no TWs

174   were related to the response to unfolded protein and a number of maturation-related terms.

175   Most of the GO-enriched terms were associated with cardiac development, including

176   muscle-structure development, extracellular-structure organization, actin-filament-based

177   processes, tissue morphogenesis, and muscle-system processes. The response to unfolded

178   protein is a coping response to mitigate or eliminate endoplasmic reticulum (ER) stress

179   caused by hypoxia[38], which could result from the high-frequency beating of the SOTRs with

7

180   TWs. To verify these findings, we performed immunostaining and quantitative polymerase

181   chain reaction (qPCR) analysis. Immunostaining for cardiac-specific markers clearly revealed

182   higher expression of β-myosin heavy chain (β-MHC), a cardiac maturity marker correlated

183   with contractile velocity, within SOTRs with one and two TWs as compared with levels

184   observed in the zero TW group (Fig. 3e and f). Moreover, analysis of mRNA expression

185   revealed a number of upregulated genes, including *MYH7* (encoding β-MHC) and genes

186   involved in sarcomere structures *(ACTN2* and *DES*), ventricular structures (*MYL2, MYL3*),

187   ER-Ca^{2+} function (*PLN*), *myoglobin* (*MB*), and *β1-adrenoceptor* (*ADRB1*). SOTRs with TWs

188   had significantly higher-fold upregulated genes as compared with those with zero TWs (Fig.

189   3e–g) due to higher beating rates during culture, which agreed well with previous reports

190   utilizing electrical stimulation at different frequencies[3,15].

191   Hematoxylin and eosin (HE) staining showed that CMs with TWs densely packed

192   with each other to a greater degree than those without TWs (Supplementary Fig. 6).

193   Moreover, SOTRs with TWs demonstrated densely packed cardiac myofilaments along the

194   ring orientation, which was also along the path of the TWs, whereas CMs in SOTRs without

195   TWs (0 TW) were randomly oriented and poorly organized (Fig. 4a and b). Additionally,

196   after a 14-day culture, CMs in SOTRs with TWs strongly expressed the α-actinin as

197   compared with those in SOTRs without TWs (Fig. 4c), in agreement to gene expression

198   (*ACTN2,* Fig. 3g). Importantly, CMs in SOTRs with TWs exhibited significantly longer

199   sarcomere length than those without TWs (1 TW: 1.71 ± 0.08 μm; 2 TWs: 1.83 ± 0.10 μm;

200   and 0 TW: 1.49 ± 0.08 μm) (Fig. 4c and d), which is closer to the sarcomere length in human

201   adult CMs[39]. Furthermore, electron microscopy indicated that cells in TW groups exhibited

202   larger sarcomeric bundles, well-defined Z disks, A-bands, and myofibrils (Fig. 4e). These

203   data suggested that CM maturation was improved within SOTRs with TWs relative to those

204   with zero TWs. Our findings confirmed the genetic and structural maturation of SOTRs with

8

205   TWs, and that faster beating rates during short-term culture could lead to higher levels of

206   maturation.

207

TWs improve bioenergetics and Ca^{2+}-handling properties

209   An extracellular-flux analyzer was used to characterize mitochondrial function in CMs within

210   SOTRs. To record the maximum activity of the electron-transport chain from adenosine

211   triphosphate (ATP) synthesis, mitochondrial ATP synthase was inhibited by oligomycin, and

212   a proton-gradient discharger was added to measure maximum mitochondrial respiration. Our

213   results indicated that the maximum respiration rate of groups with two TWs was significantly

214   higher than that observed in groups with zero or one TW (Fig. 5a and b), indicating that a

215   higher number of TWs led to increased mitochondrial activity.

216   Because human CMs rely on Ca^{2+} influx from the sarcoplasmic reticulum (SR) for

217   contraction, we investigated SR function by applying caffeine to SOTRs in order to open SR

218   ryanodine channels[3]. Although all groups responded to the addition of 5 mM caffeine (Fig. 5c

219   and d), SOTRs with two TWs exhibited significantly higher-intensity changes than groups

220   with zero TWs, indicating a higher maturation level in Ca^{2+}-handling properties and agreeing

221   well with gene-expression results. Additionally, we recorded the contractile force of SOTRs

222   using a mechanical tester (Fig. 5e and f), revealing that SOTRs with either zero or two TWs

223   generated active forces that increased along with an applied stretching force in a Frank–

224   Starling-like fashion[40]. Moreover, the group with two TWs generated forces with larger

225   amplitude than that in the group with zero TWs (2 TWs: 0.54 ± 0.15 mN/mm^2; 0 TW: $0.23 \pm$

226   0.12 mN/mm^2).

227

228   **Discussion**

9

229   Excitation-contraction coupling is important for CM development and function[41], and beating

230   rate might play an important role in cardiac maturation. The human fetal heartbeat increases

231   linearly during embryonic development from ~1 Hz to ~3 Hz within 9 weeks *in utero*[42,43].

232   hiPSC-CMs functionally and morphologically resemble fetal CMs; however, the average

233   beating rate of hiPSC-CMs is much lower than human fetal CMs. Previous studies promoted

234   CM maturation by increasing their beating rates; however, high beat rates of hiPSC-CMs

235   could only be achieved by applying high frequency electrical stimulation[3,13,15], sustainable

236   application of which is technically challenging and may cause potential side effects,

237   including pH shift, ROS generation, electrolysis[19], and cell damage[17].

238   In the present study, we created SOTRs with spontaneously generated TWs capable of

239   sustainably causing CMs to beat at high frequencies (up to 4 Hz) in the absence of external

240   stimulation. We found that CMs trained with TWs demonstrated dramatically improved

241   structural maturation, enhanced cardiac gene expression, and Ca^{2+}-handling properties in a

242   frequency dependent manner. Because this activity might also cause hypoxia in SOTRs, in

243   the future, an enhanced oxygen supply, such as that afforded by dynamic culture[5], can be

244   utilized during SOTR culture. Additionally, although the CMs trained by TWs remained less

245   mature relative to those generated by state-of-art methods[10,13,44], the maturation level afforded

246   by TWs could be further improved by changing the stimulation window/duration and

247   improving the beating frequency.

248   SOTRs were formed through a one-step, gel-free method utilizing a

249   polydimethylsiloxane (PDMS) mold and commercially available Petri dishes. SOTR

250   formation required <2 days, much shorter than the previously reported tissue-ring formation

251   time (~7–14 days)[21,45] due to multiple factors, including the use of gel-free medium, the low-

252   attachment surface of the culture dish, and the ability of the CMs to aggregate into a 3D

253   construct. This new methodology could be an important complement to current widely used

10

254   methods[3,19,21,25], and the rapid formation of the ring organoid might be important for future

255   mass production for drug-screening applications.

256   Given the large cell number required for SOTR formation in one well (4×10^5 cells),

257   it remains difficult to achieve high-throughput assessment similar to those previously

258   reported creating 200 tissue constructs per million cardiac cells[46]. Further optimizations are

259   needed to scale down the PDMS mold and reduce the plated cell number. Additionally,

260   because force generation is the primary function of CMs, force quantifications have been

261   recently utilized to assess drug-related effects[46,47]; therefore, future mold design for SOTR

262   formation might include a force transducer[48], such as an elastic silicone pillar, capable of

263   offering multiple parameters for more relevant assessment of drug response to pharmacologic

264   agents. Furthermore, since the electrical pacing could be controlled with different loading

265   level (by gradually increasing or decreasing frequency, or by tuning on/off region of

266   stimulation over time)[13,46], it would be useful to develop SOTR with controllable stimulation.

267   SOTRs with controllable silicone pillar could be used to regulate the frequency of TWs in

268   real-time.

269   It remains an open question as to what degree of CM maturation is necessary for

270   regenerative applications[49], such as injection into or engraftment onto an infarcted heart. The

271   various maturation levels of SOTRs under different TW-training levels might offer

272   preconditioned CMs for delivery into an infarcted myocardium, thereby allowing studies of

273   how CM maturation affects therapeutic efficacy.

274   The key factors necessary for the sustained TWs were the closed-loop topology and

275   the electric excitability of the enclosed cells. It could be that SOTRs with TWs can be created

276   using other electrically active cells, such as neurons and retina cells. The looped TW might

277   be useful for promoting the maturation of these cell types, which have previously been

278   matured by electrical stimulation[50-53]. Moreover, because the frequency of the TWs within the

11

279   SOTRs can be adjusted by changing SOTR diameter, and given that the TWs could be

280   sustained for >89 days, it might be possible to create pacemaker tissue with an adjustable

281   beat rate for use as an *in vitro* model for drug assessment or potentially for *in vivo* heart

282   pacing.

283   In conclusion, we found that TWs could be spontaneously generated and maintained

284   within a SOTR comprising hiPSC-CMs, and that the TWs were able to make the CMs beat at

285   a high frequency comparable to that found *in utero* during embryonic development.

286   Moreover, the TWs promoted frequency dependent structural and functional maturation of

287   the CMs, thereby offering a supplementary approach to electrical-stimulation-based

288   maturation of electrically active cell types.

289

290   **Methods**

291   **Differentiation and culture of hiPSC-CMs**

292   GCaMP3-positive hiPSCs (253G1) were cultured[54] and differentiated[55] according to

293   previously published methods[54,56]. All experiments involving the use of hiPSCs were

294   performed following Kyoto University and Osaka University guidelines. After 30 to 50 days

295   of differentiation, CM colonies floating in medium were collected and dissociated into a

296   single-cell suspension by stirring for between 1 h and 2 h in protease solution [0.1%

297   collagenase type I, 0.25% trypsin, 1 U/mL DNase I, 116 mM NaCl, 20 mM HEPES, 12.5

298   mM NaH_2PO_4, 5.6 mM glucose, 5.4 mM KCl, and 0.8 mM $MgSO_4$ (pH 7.35)][56.] The CM

299   purity was characterized with Flow Cytometry and the CMs with high purity (> 85 %) were

300   used for following experiments.

301

302   **Device manufacture**

303   PDMS (SYLGARD 184; Dow Corning, Midland, MI, USA) blocks were punched using a

304   tissue puncher (Thermo Fisher Scientific, Waltham, MA, USA) to an inner diameter of 8 mm.

305   After removal of the redundant central pillar, the remaining PDMS wells were collected, and

306   PDMS wells and pillars with different diameters were centrally aligned and attached to the

307   bottom of 24-well ultra-low attachment plates (Corning, Corning, NY, USA) as shown in

308   Supplementary Fig. 1c. For micro-electrode array (MEA; Multi Channel Systems, Reutlingen,

309   Germany) recording, the PDMS well and pillars were mounted to the MEA surface using

310   silicone glue (Shin-Etsu Chemical, Tokyo, Japan) to fix the well and pillar to the bottom of

311   the well. After drying and treatment with UV light for 30 min, the PDMS wells were ready

312   for CM culture.

313

314   **SOTR generation**

315   Before cell seeding, single CMs were filtered using a 40-μm cell strainer (BD Falcon; Becton

316   Dickenson, Franklin Lakes, NJ, USA) and resuspended at a density of 2×10^6 cells/mL in

317   serum-supplemented cardiac differentiation medium (Sigma-Aldrich, St. Louis, MO, USA)

318   containing 20% fetal bovine serum (FBS; Gibco, Grand Island, NY, USA), 1% minimum

319   essential medium non-essential amino acid solution (Sigma-Aldrich), 1% penicillin-

320   streptomycin (Gibco), 2 mM L-glutamine (Sigma-Aldrich), 0.001% 2-mercaptoethanol

321   (Gibco), and 0.005 N NaOH along with 10 ng/mL bone morphogenetic protein 4 (R&D

322   Systems, Minneapolis, MN, USA). 4×10^5 cells were plated in each PDMS culture well with

323   3-mm pillar. For wells with other diameters, the cell number was fixed to 4×10^5 or

324   proportional to the diameter. After plating, CMs settled in the wells, aggregated, and

325   congregated around the central pillar to form densely packed tissue rings within 2 days. The

326   medium was changed to serum-free medium (cardiac differentiation medium without FBS)

327   from day 2. After that, fresh medium was changed every 4 days. Before medium changing,

13

328   the fresh medium was pre-warmed to 37 degree. The dishes were placed on top of a pre-

329   warmed metal block during medium changing. The medium was pipetted gently and slowly

330   into the wells.

331

332   **Optical mapping and measurement**

333   Progression of tissue assembly was observed using a fluorescence microscope (Olympus

334   IX71; Olympus, Tokyo, Japan) equipped with a charge-coupled device (CCD) camera

335   (Exiblue; Qimaging, Surrey, BC, Canada; or DP74; Olympus). GCaMP3 was excited from

336   450 nm to 490 nm, and fluorescence images of GCaMP3-positive CMs were recorded with

337   8×8 binning of CCD pixels at 30 frames/s. Images were processed to obtain data using

338   ImageJ (NIH, Bethesda, MD, USA) and MATLAB (R2014b; MathWorks, Natick, MA, USA)

339   using a customized program. Activation-time mapping was performed using a custom plug-in

340   in ImageJ, as previously described[57].

341

342   **Transient and electrophysiological Ca^{2+} characterization**

343   Ca^{2+} transience was recorded by fluorescence imaging of GCaMP3-positive CMs with the

344   same experimental setup as that described for optical mapping and measurement. To

345   characterize the spontaneous beating of SOTRs, TWs were removed from the SOTRs 1 day

346   before recording by emerging the SOTRs into medium at room temperature for 1 min. The L-

347   type Ca^{2+}-channel blocker verapamil (1 mM; Sigma-Aldrich) and 5 mM caffeine (Wako Pure

348   Chemical Industries, Ltd. Osaka, Japan) were added directly to the chamber containing the

349   SOTRs during imaging, as described in the figure legends.

350   Extracellular recording of field potentials (FPs) was performed using an MEA data-

351   acquisition system (USB-ME64; Multi Channel Systems). Signals were recorded from days 5

352   and 6 after CM seeding, and data were collected and processed using MC_Rack (Multi

353   Channel Systems) or LabChart (ADInstruments, Dunedin, New Zealand). The amplitude, QT

354   interval, and beat rate were determined by analyzing the wave form of the FP.

355

356   **Histology**

357   SOTRs were rinsed three times with phosphate-buffered saline (PBS), fixed in 4%

358   paraformaldehyde (PFA) in PBS for 30 min, and embedded in paraffin. Thin sections were

359   sliced and stained with HE (Muto Chemical Corporation, Tokyo, Japan), and observation was

360   carried out using a CKX41 microscope (Olympus).

361

362   **Immunostaining and imaging**

363   SOTRs were fixed in 4% PFA at room temperature for 30 min, permeabilized with 0.5% (v/v)

364   Triton X-100 in Dulbecco's (D)-PBS at room temperature for 1 h, and incubated in blocking

365   solution [0.1% (v/v) Tween-20, 5% (v/v) normal donkey serum, 3% (v/v) bovine serum

366   albumin, and 5% (v/v) normal goat serum in D-PBS] at 4°C for 16 h. SOTRs were then

367   incubated with the primary antibodies anti-troponin T2 (TnT2; mouse monoclonal IgG; 1:200;

368   SC-20025; Santa Cruz Biotechnology, Dallas, TX, USA), anti-α-actinin (mouse monoclonal

369   IgG, 1:1000; A7811; Sigma-Aldrich), or anti-β-MHC (mouse MYH7 monoclonal IgM, 1:100;

370   SC-53089; Santa Cruz Biotechnology) at 4°C overnight. SOTRs were then rinsed with PBS

371   and incubated with secondary antibodies diluted 1:300 in blocking buffer (Alexa Fluor 594

372   anti-mouse IgG; 715-586-150; and DyLight-594 anti-mouse IgM; 715-516-020; Jackson

373   ImmnoResearch, West Grove, PA, USA) at room temperature for 1 h. 4′-6-Diamidino-2-

374   phenylindole (DAPI; 300 nM; Wako Pure Chemical Industries, Ltd.) was used to counterstain

375   nuclei at room temperature for 30 min, after which images were captured using a confocal

376   microscope (FV1200; Olympus). CM orientation within SOTRs was determined using the

377   Fourier component analysis plugin "Directionality" in ImageJ[47] (NIH) that calculated the

15

378   orientation distribution for the red color channel. Fluorescence quantification of β-MHC was

379   performed by calculating the gray value averaged over the area in all sample groups, with all

380   the fluorescence values were normalized to that of zero TW group.

381

382   **Transmission electron microscopy (TEM)**

383   SOTRs were washed with 0.1 M Sorenson's buffer (pH 7.4) twice and fixed with 2.5%

384   glutaraldehyde (Sigma-Aldrich) in 0.1 M Sorenson's buffer (pH 7.4), after which samples

385   were post-fixed with 1% OsO_4 in Sorrenson's buffer. The samples were then embedded,

386   sliced, and stained with lead citrate and examined under a JEOL1010 transmission electron

387   microscope (JEOL Ltd., Tokyo, Japan).

388

389   **Mitochondrial respiration assay**

390   Mitochondrial function was analyzed using a Seahorse XF96 extracellular flux analyzer

391   (Agilent Technologies, Carlsbad, CA, USA). After a 14-day culture, SOTRs were dissociated

392   into a single-cell suspension by stirring for 30 min in protease solution, followed by cell

393   seeding onto a cell-culture microplate (Agilent Technologies) at a density of 20,000 cells per

394   XF96 well. OCR assays were performed 3 days after seeding, and culture medium was

395   changed to the base medium (Seahorse XF assay media supplemented with 1 mM sodium

396   pyruvate; Life Technologies, Carlsbad, CA, USA). Substrates and inhibitors were injected

397   during measurements at a final concentrations of 3.5 μM 4-(trifluoromethoxy)

398   phenylhydrazone (FCCP; Seahorse Bioscience, Billerica, MA, USA), 1 μM oligomycin, 0.5

399   μM antimycin, and 0.5 μM rotenone for the MitoStress assay.

400

401   **Flow Cytometry**

402 Before used for generating SOTRs, hiPSCs-CMs fixed in 4% PFA at room temperature for

403 30 min, permeabilized with 0.5% v/v Triton X-100 in Dulbecco's (D)-PBS at room

404 temperature for 30 min, incubated with anti-cTnT antibodies (mouse monoclonal IgG, 1:200;

405 Santa Cruz Biotechnology: SC-20025) or isotype-matched antibodies (BD Phosphoflow:

406 557782) at 37 °C for 30 min, washed with D-PBS, and then incubated with Alexa Fluor 488

407 anti-mouse IgG (1:500; Jackson ImmnoResearch: 715-546-150). Cells were then washed

408 twice with D-PBS and analyzed using a FACS Canto II flow cytometer (BD Biosciences,

409 USA) and the FlowJo software (Treestar Inc., USA). Data shown are representative of

410 five independent experiments.

411

412 **Contractility analysis**

413 SOTR contractility was measured using a micron-scale mechanical-testing system

414 (MicroSquisher; CellScale Biomaterials Testing, Waterloo, ON, Canada). TWs were stopped

415 by exchanging medium at room temperature 1 day before measurement, and the SOTR was

416 removed from the pillar and fixed on a stage. A cantilever beam with a diameter of 0.30 mm

417 was pressed onto the SOTR, with the force calculated by cantilever-beam deflection in

418 response to differential displacement. All samples were tested at 37°C.

419

420 **qPCR**

421 Total RNA in SOTRs was harvested using Trizol reagent (Life Technologies) according to

422 manufacturer instructions, and RNA concentration was determined using a NanoDrop1000

423 spectrophotometer (Thermo Fisher Scientific). cDNA was synthesized with a first-strand

424 synthesis kit (TaKaRa, Shiga, Japan) and analyzed by qPCR using SYBR Green PCR master

425 mix (Life Technologies) and the qBiomarker validation PCR array (IPHS-102A; Qiagen,

426 Hilden, Germany) in a 96-well format according to manufacturer instructions. Cycling

17

427 conditions were set as follows: initial denaturation at 95°C for 10 min, followed by 40 cycles

428 at 95°C for 15 s and 60°C for 70s. Reactions were performed in a StepOnePlus real-time PCR

429 system (Life Technologies). Gene expression was determined using the $2^{-\Delta\Delta Ct}$ method and

430 relative to *glyceraldehyde 3-phosphate dehydrogenase* expression. Heatmaps were created by

431 the "pheatmap" package (https://cran.r-project.org/web/packages/pheatmap/index.html), and

432 clustering order was produced using the Ward.D clustering algorithm (https://stat.ethz.ch/R-

433 manual/R-devel/library/stats/html/hclust.html).

434

435 **RNA quantification and qualification for RNA sequencing**

436 RNA degradation and contamination was monitored on 1% agarose gels. RNA purity was

437 determined using a NanoPhotometer spectrophotometer (Implen, Westlake Village, CA,

438 USA). RNA concentration was measured using a Qubit RNA assay kit in a Qubit 2.0

439 fluorometer (Life Technologies). RNA integrity was assessed using the RNA Nano 6000

440 assay kit and the Agilent Bioanalyzer 2100 system (Agilent Technologies).

441

442 **Library preparation for RNA sequencing**

443 A total of 1.5 μg RNA per sample was used as input material for RNA sample preparations.

444 Sequencing libraries were generated using a NEBNext UltraTM RNA library prep kit

445 Illumina (New England Biolabs, Ipswich, MA, USA) according to manufacturer instructions,

446 and index codes were added to attribute sequences to each sample. Briefly, mRNA was

447 purified from total RNA using poly-T oligo-attached magnetic beads, and fragmentation was

448 performed using divalent cations under an elevated temperature in NEBNext First Strand

449 Synthesis reaction buffer (5×; New England Biolabs). First-strand cDNA was synthesized

450 using a random hexamer primer and M-MuLV reverse transcriptase (RNase H−; New

451 England Biolabs). Second-strand cDNA synthesis was subsequently performed using DNA

18

452   polymerase I and RNase H. Remaining overhangs were converted into blunt ends via

453   exonuclease/polymerase activities. After adenylation of the 3′ ends of the DNA fragments,

454   NEBNext Adaptor (New England Biolabs) with a hairpin loop structure was ligated to

455   prepare for hybridization. To select cDNA fragments of the correct length, the library

456   fragments were purified using the AMPure XP system (Beckman Coulter, Beverly, MA,

457   USA), after which 3 µL USER enzyme (New England Biolabs) was incubated with size-

458   selected, adaptor-ligated cDNA at 37°C for 15 min, followed by 5 min at 95°C. PCR was

459   performed using a Phusion high-fidelity DNA polymerase, universal PCR primers, and an

460   Index (X) primer (New England Biolabs). Products were purified (AMPure XP; Beckman

461   Coulter), and library quality was assessed using the Agilent Bioanalyzer 2100 system

462   (Agilent Technologies).

463

464   **Clustering and sequencing**

465   Clustering of the Index-coded samples was performed on a cBot cluster generation system

466   using a HiSeq 4000 PE cluster kit (Illumia, San Diego, CA, USA) according to manufacturer

467   instructions. After cluster generation, the library preparations were sequenced on an Illumina

468   Hiseq 4000 platform (Illumina), and 150-bp paired-end reads were generated.

469   After quality control, the paired-end reads were aligned to the hg19 human reference

470   genome   (UCSC;   https://genome.ucsc.edu/)   using   TopHat   (v2.0.12;

471   https://ccb.jhu.edu/software/tophat/index.shtml)[48]. We quantified the relative expression level

472   as $\log_2(FPKM + 1)$ to perform PCA analysis and hierarchical clustering. Uniquely mapped

473   reads counted by HTSeq[49] were used to conduct differential-expression analysis in DEseq2[50].

474   A total of 349 gens (p<0.05, fold change>1.5) were selected for the GO analysis. We plotted

475   heatmaps   using   the   "pheatmap"   package   in   R   (https://cran.r-

476   project.org/web/packages/pheatmap/index.html) and performed GO enrichment analysis

477   using Metascape[58] (http://metascape.org/).

478

479   **Statistical analysis**
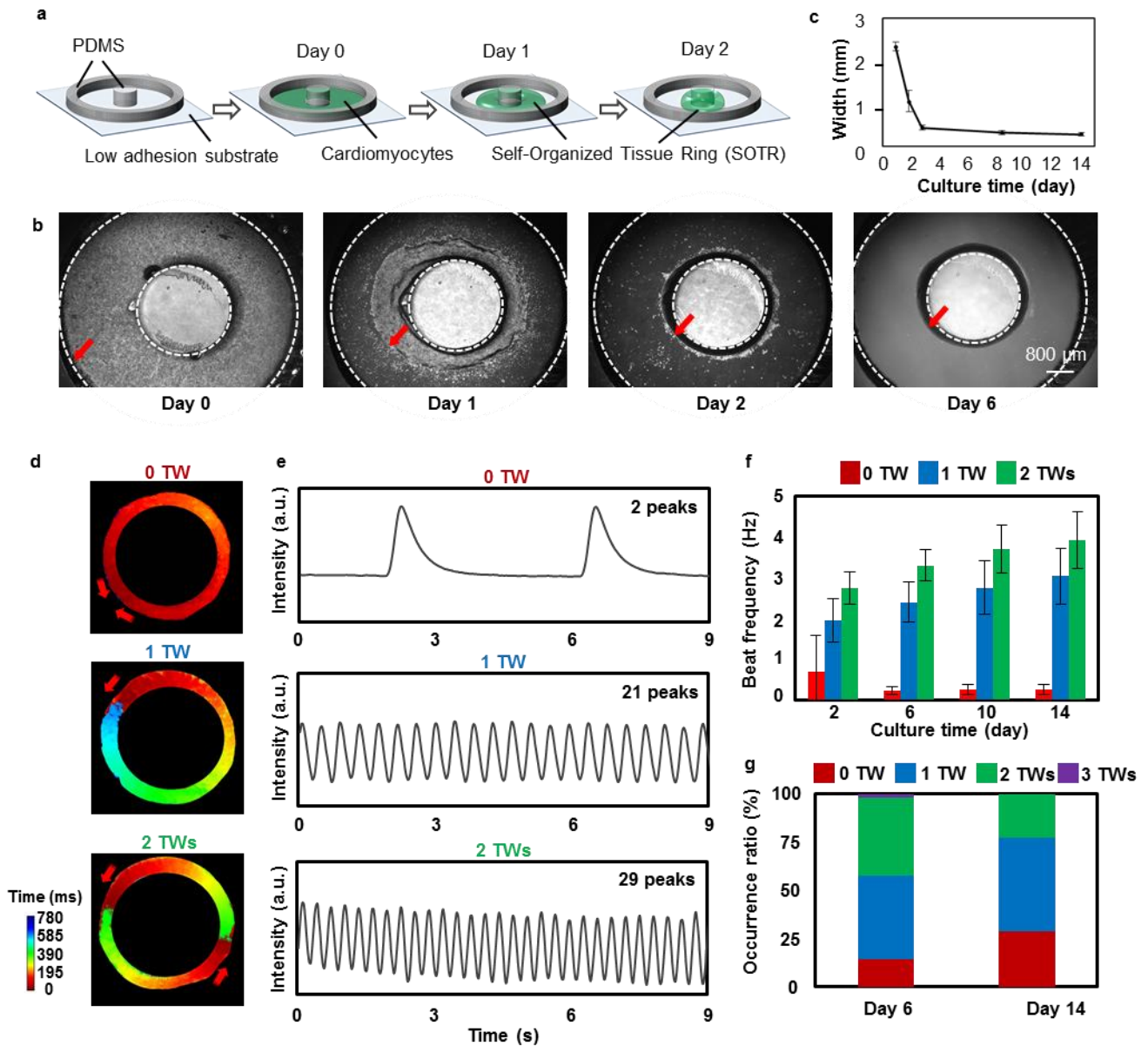
480   All quantitative data are presented as the mean ± standard deviation of the mean (mean ± s.d.).

481   The differences between experimental groups were analyzed by Student's *t* test (between two

482   groups) or one-way analysis of variance, followed by Tukey's post hoc test (among three

483   groups). A $P < 0.05$ was considered statistically significant.

484

Figure 1. TWs promoted rapid beating of cells in SOTRs. (a) Schematic describing SOTR formation. (b) Bright-field images of hiPSC-CMs in the template. The red arrows indicate the edge of cardiac tissues in the template, and the dashed lines indicated the PDMS block and pillar boundaries, respectively. Pillar diameter = 3mm. (c) Quantification of the width of the SOTRs on the indicated culture day (mean ± s.d.; $n = 4$). (d) Activation map of GCaMP3-positive SOTRs with zero, one, or two TWs. The red arrows indicate the propagation direction of the action potential. (e) GCaMP3-fluorescence signal at a fixed position on the ring of SOTRs with zero, one, or two TWs on day 6. (f) Beat rates of SOTRs at different

21

493   culture times (mean ± s.d.; 2 TWs: $n = 10$; 1 TW: $n = 12$; 0 TWs: $n = 8$). (g) The percentage

494   of occurrence for different numbers of TWs on days 6 ($n = 204$) and 14 ($n = 186$),

495   respectively.
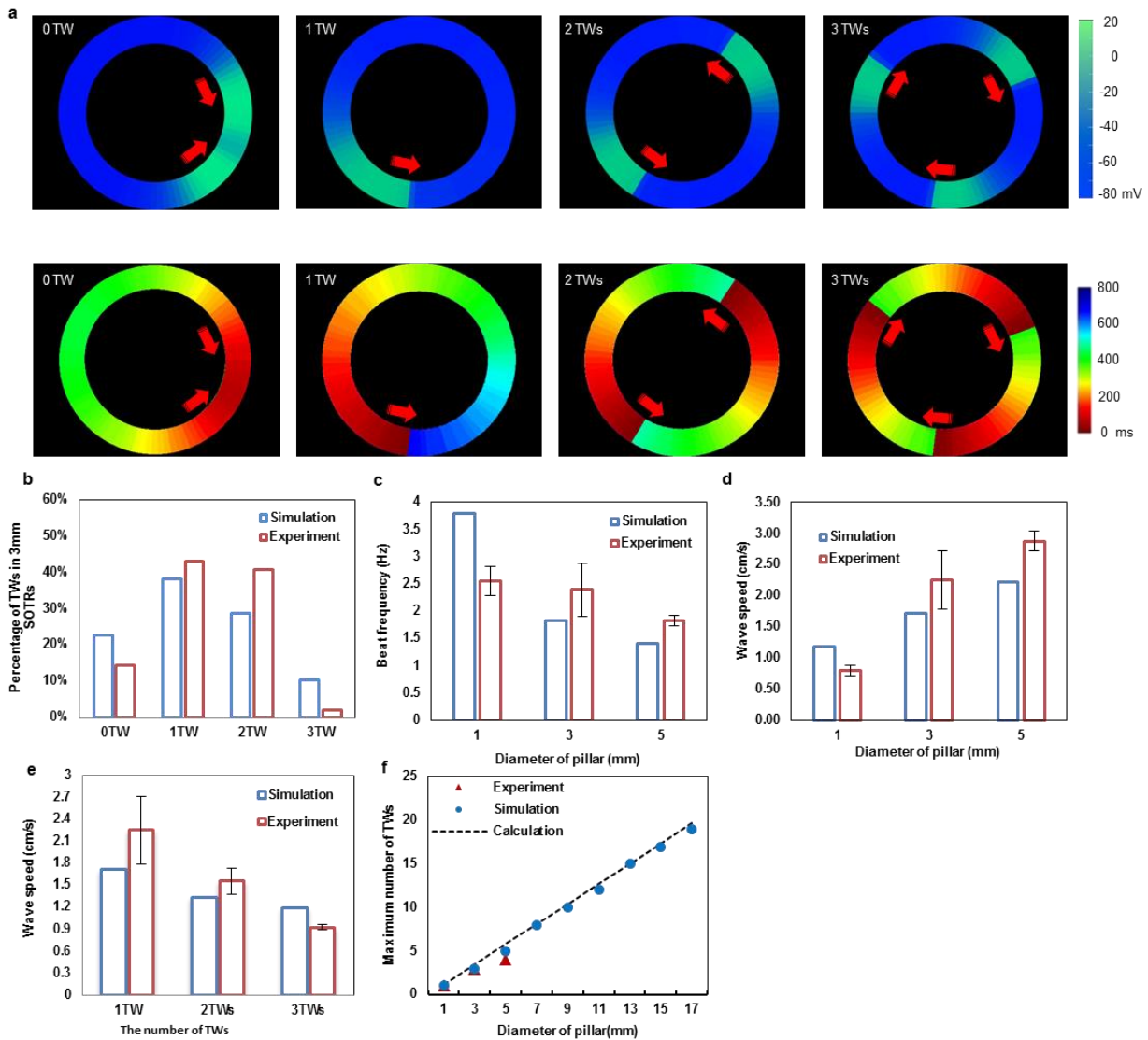
496

497   **Figure 2. Accurate reproduction of TW features in SOTRs using a mathematical model.**

498   (a) Examples of simulation results of the model (upper panel) and the activation map (lower

499   panel). For the group with zero TWs, an action potential initiates from the left position of the

500   ring and propagates in the opposite directions along the ring, after which the two waves meet

501   and annihilate on another. The process will starts again with new waves initiating at the same

502   position periodically. For groups with one, two, or three TWs, stable TWs travel around the

503 ring. Membrane potential and activation time are color coded. (b) The percentage of stable

504 TWs in SOTRs at day 6 (diameter = 3 mm; $n = 60$ in the simulation and $n = 204$ in the

505 experiment). (c) Beat rate (Hz) of CMs in SOTRs with one TW at day 6 for different pillar

506 diameters [experiment: 1-mm SOTR ($n = 4$); 3-mm SOTR ($n = 12$); 5-mm SOTR ($n = 10$)].

507 (d) Similar information shown in (c) but with TW speed. (e) Speeds of one, two, or three

508 TWs in SOTRs with a pillar diameter of 3 mm [experiment: mean ± s.d.; 3 TWs ($n = 4$); 2

509 TWs ($n = 10$); 1 TW ($n = 12$)]. (f) The maximum number of TWs in SOTRs with different

510 pillar diameters.

511

512
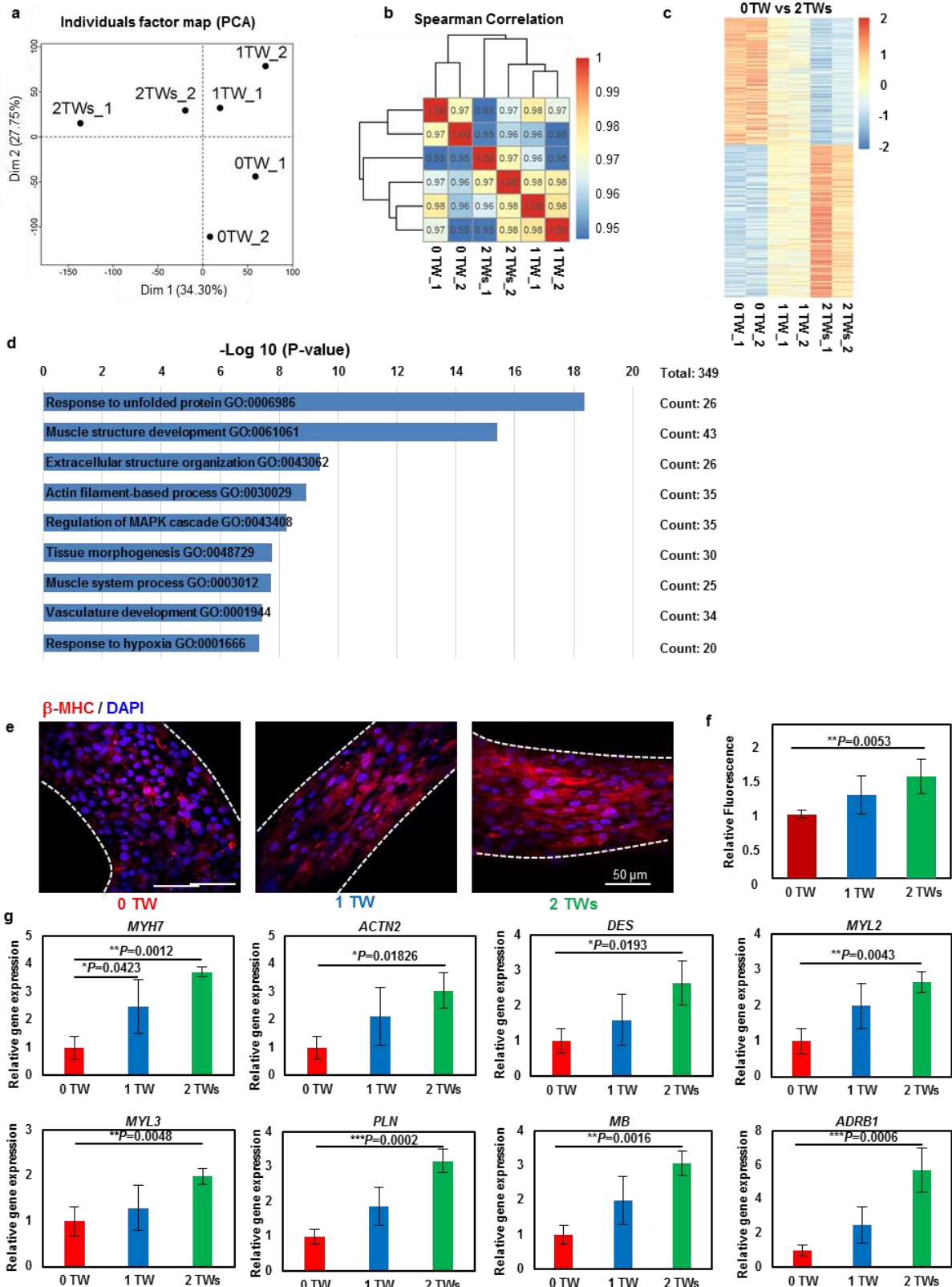
Figure 3. TWs upregulate cardiac-specific gene expression. (a) PCA of SOTRs with or

without TWs based on RNA-sequencing data. (b) Heatmap showing hierarchical clustering of

515   the correlation matrix resulting from comparison of expression values for each sample.

516   Correlations calculated using Spearman correlation. (c) Heatmap showing the relative

517   expression levels (z-score) of 349 genes from SOTRs with TWs (1 and 2 TWs) as compared

518   with SOTRs with zero TWs. (d) GO categories significantly enriched for genes upregulated

519   in SOTRs with two TWs as compared with SOTRs with zero TWs. Genes with fold

520   changes > 1.5 and a P < 0.05 were analyzed. Enriched terms are listed. (e) Representative

521   confocal images of SOTRs with zero, one, or two TWs on day 14. CMs were stained with

522   anti-β-MHC (red) and DAPI (blue). (f) Quantification of β-MHC levels in SOTRs on day 14.

523   Total integrated fluorescence of β-MHC was normalized to that of SOTRs with zero TWs

524   (mean ± s.d.; $n = 4$). **$P < 0.01$. (g) The expression of cardiac-specific genes in SOTRs 14

525   days after cell seeding (mean ± s.d.; $n = 4$). *$P < 0.05$; **$P < 0.01$; ***$P < 0.001$.

526
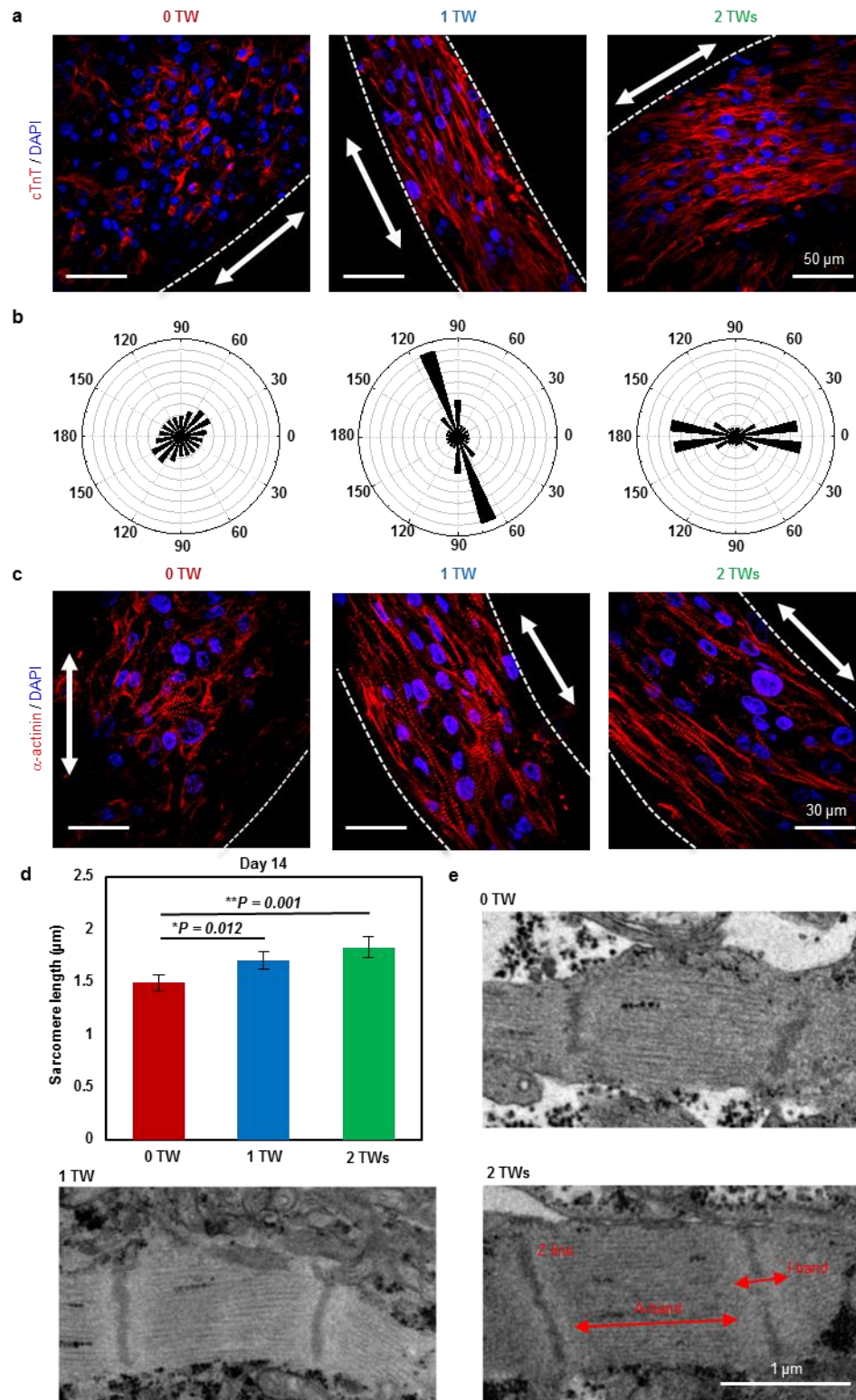
Figure 4. TWs promote CM alignment. (a) Representative confocal images of SOTRs with zero, one, or two TWs. CMs were stained with anti-TnT2 (red) and DAPI (blue), revealing CM alignment in TW samples. Arrows mark the ring orientation. (b) Angular graph based on

531   Fourier component analysis of TnT2 orientation distribution. (c) Representative confocal

532   images of stained SOTRs with different TWs (red: α-actinin; blue: DAPI). Arrows mark the

533   ring orientation. (d) Sarcomere lengths of CMs within SOTRs on day 14 [mean ± s.d.; 0

534   TWs ($n = 5$); 1 TW ($n = 5$); 2 TWs ($n = 4$)]. *$P < 0.05$; **$P < 0.01$. (e) TEM analysis of

535   SOTRs on day 14.

536

537
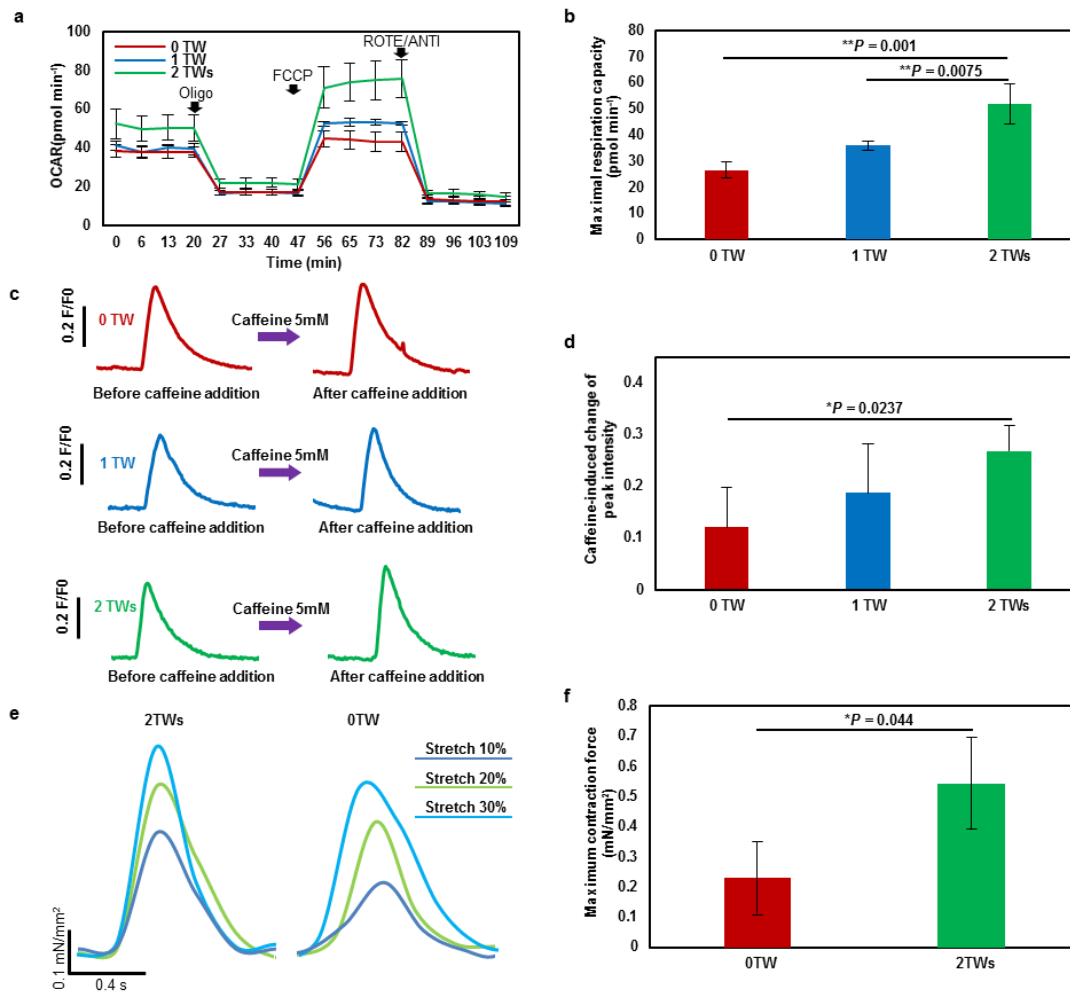
Figure 5. TWs improve Ca^{2+}-handling properties. (a) Results of OCR assays. Olig, oligomycin; FCCP, carbonyl cyanide-4-(trifluoromethoxy) phenylhydrazone; ROTE/ANTI, rotenone and antimycin A. (b) Quantification of maximal respiration capacity (mean ± s.d.; n = 4). **$P < 0.01$. (c) Representative traces of Ca^{2+} transient following administration of 5 mM caffeine to CMs in SOTRs with zero TWs, one TW, and two TWs at day 7. SOTRs were immersed in room temperature medium to stop TWs on day 6. (d) Caffeine-induced change in peak intensity in different groups (mean ± s.d.; n = 6). *$P < 0.05$. (e) Force traces of SOTRs during progressive stretching. (f) Maximum contractile force of SOTRs (mean ± s.d.; $n = 3$). *$P < 0.05$.

547

Reference

1   Karakikes, I., Ameen, M., Termglinchan, V. & Wu, J. C. Human Induced Pluripotent Stem Cell–Derived Cardiomyocytes Insights Into Molecular, Cellular, and Functional Phenotypes. *Circulation Research.* **117**, 80-88 (2015).

2   Dolnikov, K. *et al.* Functional properties of human embryonic stem cell–derived cardiomyocytes: intracellular Ca2+ handling and the role of sarcoplasmic reticulum in the contraction. *Stem cells.* **24**, 236-245 (2006).

3   Nunes, S. S. *et al.* Biowire: a platform for maturation of human pluripotent stem cell-derived cardiomyocytes. *Nat. Methods.* **10**, 781-787 (2013).

4   Davis, R. P. *et al.* Cardiomyocytes derived from pluripotent stem cells recapitulate electrophysiological characteristics of an overlap syndrome of cardiac sodium channel disease. *Circulation.* **125**, 3079-3091 (2012).

5   Jackman, C. P., Carlson, A. L. & Bursac, N. Dynamic culture yields engineered myocardium with near-adult functional output. *Biomaterials.* **111**, 66-79 (2016).

6   Ulmer, B. M. *et al.* Contractile Work Contributes to Maturation of Energy Metabolism in hiPSC-Derived Cardiomyocytes. *Stem cell reports.* **10**, 834-847 (2018).

7   Shadrin, I. Y. *et al.* Cardiopatch platform enables maturation and scale-up of human pluripotent stem cell-derived engineered heart tissues. *Nature communications.* **8**, 1825 (2017).

8   Gao, L. *et al.* Myocardial Tissue Engineering With Cells Derived From Human-Induced Pluripotent Stem Cells and a Native-Like, High-Resolution, 3-Dimensionally Printed Scaffold. *Circulation Research.* **120**, 1318-1325 (2017).

9   Parikh Shan, S. *et al.* Thyroid and Glucocorticoid Hormones Promote Functional T-Tubule Development in Human-Induced Pluripotent Stem Cell–Derived Cardiomyocytes. *Circulation Research.* **121**, 1323-1330 (2017).

10   Herron, T. J. *et al.* Extracellular matrix–mediated maturation of human pluripotent stem cell–derived cardiac monolayer structure and electrophysiological function. *Circulation: Arrhythmia and Electrophysiology.* **9**, e003638 (2016).

11   Brevet, A., Pinto, E., Peacock, J. & Stockdale, F. E. Myosin synthesis increased by electrical stimulation of skeletal muscle cell cultures. *Science.* **193**, 1152-1154 (1976).

12   McDonough, P. M. & Glembotski, C. Induction of atrial natriuretic factor and myosin light chain-2 gene expression in cultured ventricular myocytes by electrical stimulation of contraction. *J. Biol. Chem.* **267**, 11665-11668 (1992).

13   Ronaldson-Bouchard, K. *et al.* Advanced maturation of human cardiac tissue grown from pluripotent stem cells. *Nature.* **556**, 239-243 (2018).

14   Nunes, S. S. *et al.* Biowire: a platform for maturation of human pluripotent stem cell-derived cardiomyocytes. *Nat Methods.* **10**, 781-787 (2013).

15   Eng, G. *et al.* Autonomous beating rate adaptation in human stem cell-derived cardiomyocytes. *Nature communications.* **7** (2016).

16   Tandon, N. *et al.* Electrical stimulation systems for cardiac tissue engineering. *Nature protocols.* **4**, 155-173 (2009).

17   Merrill, D. R., Bikson, M. & Jefferys, J. G. R. Electrical stimulation of excitable tissue: design of efficacious and safe protocols. *J. Neurosci. Methods.* **141**, 171-198 (2005).

18   Hirt, M. N. *et al.* Functional improvement and maturation of rat and human engineered heart tissue by chronic electrical stimulation. *Journal of molecular and cellular cardiology.* **74**, 151-161 (2014).

19   Godier-Furnémont, A. F. *et al.* Physiologic force-frequency response in engineered heart muscle by electromechanical stimulation. *Biomaterials.* **60**, 82-91 (2015).

596 20 van Meer, B. J., Tertoolen, L. G. & Mummery, C. L. Measuring physiological responses of
597   human pluripotent stem cell derived cardiomyocytes to drugs and disease. *STEM CELLS.* **34**,
598   2008-2015 (2016).
599 21 Zimmermann, W.-H. *et al.* Tissue engineering of a differentiated cardiac muscle construct.
600   *Circulation research.* **90**, 223-230 (2002).
601 22 Dhein, S. *et al.* Mechanical control of cell biology. Effects of cyclic mechanical stretch on
602   cardiomyocyte cellular organization. *Progress in biophysics and molecular biology.* **115**, 93-
603   102 (2014).
604 23 Li, Y. *et al.* Chinese-Noodle-Inspired Muscle Myofiber Fabrication. *Advanced Functional*
605   *Materials.* **25**, 5999-6008 (2015).
606 24 Tulloch, N. L. *et al.* Growth of engineered human myocardium with mechanical loading and
607   vascular coculture. *Circulation research.* **109**, 47-59 (2011).
608 25 Mihic, A. *et al.* The effect of cyclic stretch on maturation and 3D tissue formation of human
609   embryonic stem cell-derived cardiomyocytes. *Biomaterials.* **35**, 2798-2808 (2014).
610 26 Shaheen, N. *et al.* Human Induced Pluripotent Stem Cell-Derived Cardiac Cell Sheets
611   Expressing Genetically Encoded Voltage Indicator for Pharmacological and Arrhythmia
612   Studies. *Stem cell reports.* **10**, 1879-1894 (2018).
613 27 Kadota, S. *et al.* Development of a reentrant arrhythmia model in human pluripotent stem
614   cell-derived cardiac cell sheets. *European heart journal.* **34**, 1147-1156 (2012).
615 28 González, H., Nagai, Y., Bub, G., Glass, L. & Shrier, A. Reentrant waves in a ring of embryonic
616   chick ventricular cells imaged with a Ca2+ sensitive dye. *BioSyst.* **71**, 71-80 (2003).
617 29 Kawatou, M. *et al.* Modelling Torsade de Pointes arrhythmias in vitro in 3D human iPS cell-
618   engineered heart tissue. *Nature communications.* **8**, 1078 (2017).
619 30 Smeets, J. L., Allessie, M. A., Lammers, W. J., Bonke, F. I. & Hollen, J. The wavelength of the
620   cardiac impulse and reentrant arrhythmias in isolated rabbit atrium. The role of heart rate,
621   autonomic transmitters, temperature, and potassium. *Circulation research.* **58**, 96-108
622   (1986).
623 31 Izumi-Nakaseko, H. *et al.* Characterization of human iPS cell-derived cardiomyocyte sheets as
624   a model to detect drug-induced conduction disturbance. *The Journal of toxicological sciences.*
625   **42**, 183-192 (2017).
626 32 Rensma, P. L., Allessie, M. A., Lammers, W. J., Bonke, F. I. & Schalij, M. J. Length of excitation
627   wave and susceptibility to reentrant atrial arrhythmias in normal conscious dogs. *Circulation*
628   *research.* **62**, 395-410 (1988).
629 33 Courtemanche, M., Keener, J. P. & Glass, L. A delay equation representation of pulse
630   circulation on a ring in excitable media. *SIAM Journal on Applied Mathematics.* **56**, 119-142
631   (1996).
632 34 Courtemanche, M., Glass, L. & Keener, J. P. Instabilities of a propagating pulse in a ring of
633   excitable media. *Physical Review Letters.* **70**, 2182 (1993).
634 35 Shaw, R. M. & Rudy, Y. Ionic mechanisms of propagation in cardiac tissue: roles of the
635   sodium and L-type calcium currents during reduced excitability and decreased gap junction
636   coupling. *Circulation research.* **81**, 727-741 (1997).
637 36 Beauchamp, P. *et al.* Electrical propagation in synthetic ventricular myocyte strands from
638   germline connexin43 knockout mice. *Circulation research.* **95**, 170-178 (2004).
639 37 Arduini, D., Rizzo, G. & Romanini, C. *Fetal cardiac function*. (Parthenon Pub. Group, 1995).
640 38 Groenendyk, J., Agellon, L. B. & Michalak, M. Coping with endoplasmic reticulum stress in
641   the cardiovascular system. *Annu. Rev. Physiol.* **75**, 49-67 (2013).
642 39 van der Velden, J., de Jong, J. W., Owen, V., Burton, P. & Stienen, G. Effect of protein kinase
643   A on calcium sensitivity of force and its sarcomere length dependence in human
644   cardiomyocytes. *Cardiovascular research.* **46**, 487-495 (2000).
645 40 Asnes, C. F., Marquez, J. P., Elson, E. L. & Wakatsuki, T. Reconstition of the Frank-Starling
646   mechanism in engineered heart tissues. *Biophys. J.* **91**, 1800-1810 (2006).

647 41 Stoppel, W. L., Kaplan, D. L. & Black Iii, L. D. Electrical and mechanical stimulation of cardiac
648   cells and tissue constructs. *Advanced Drug Delivery Reviews.* **96**, 135-155 (2016).
649 42 Lindsley, D. B. Heart and brain potentials of human fetuses in utero. *The American Journal of*
650   *Psychology.* **55**, 412-416 (1942).
651 43 DuBose, T. J., Cunyus, J. A. & Johnson, L. F. Embryonic heart rate and age. *Journal of*
652   *Diagnostic Medical Sonography.* **6**, 151-157 (1990).
653 44 Zhang, D. *et al.* Tissue-engineered cardiac patch for advanced functional maturation of
654   human ESC-derived cardiomyocytes. *Biomaterials.* **34**, 5813-5820 (2013).
655 45 Gwyther, T. A. *et al.* Engineered vascular tissue fabricated from aggregated smooth muscle
656   cells. *Cells Tissues Organs.* **194**, 13-24 (2011).
657 46 Boudou, T. *et al.* A microfabricated platform to measure and manipulate the mechanics of
658   engineered cardiac microtissues. *Tissue Engineering Part A.* **18**, 910-919 (2011).
659 47 Agarwal, A., Goss, J. A., Cho, A., McCain, M. L. & Parker, K. K. Microfluidic heart on a chip for
660   higher throughput pharmacological studies. *Lab on a Chip.* **13**, 3599-3608 (2013).
661 48 Marquez, J. P. *et al.* High-throughput measurements of hydrogel tissue construct mechanics.
662   *Tissue Engineering Part C: Methods.* **15**, 181-190 (2009).
663 49 Laflamme, M. A. & Murry, C. E. Heart regeneration. *Nature.* **473**, 326-335 (2011).
664 50 Sato, T. *et al.* Effect of electrical stimulation on IGF-1 transcription by L-type calcium
665   channels in cultured retinal Müller cells. *Japanese journal of ophthalmology.* **52**, 217-223
666   (2008).
667 51 Ito, A. *et al.* Induction of functional tissue-engineered skeletal muscle constructs by defined
668   electrical stimulation. *Scientific reports.* **4**, 4781 (2014).
669 52 Kamioka, H., Maeda, E., Jimbo, Y., Robinson, H. P. & Kawana, A. Spontaneous periodic
670   synchronized bursting during formation of mature patterns of connections in cortical
671   cultures. *Neurosci. Lett.* **206**, 109-112 (1996).
672 53 Huang, Y. J., Wu, H. C., Tai, N. H. & Wang, T. W. Carbon nanotube rope with electrical
673   stimulation promotes the differentiation and maturity of neural stem cells. *Small.* **8**, 2869-
674   2877 (2012).
675 54 Shiba, Y. *et al.* Human ES-cell-derived cardiomyocytes electrically couple and suppress
676   arrhythmias in injured hearts. *Nature.* **489**, 322-325 (2012).
677 55 Minami, I. *et al.* A small molecule that promotes cardiac differentiation of human
678   pluripotent stem cells under defined, cytokine-and xeno-free conditions. *Cell Rep.* **2**, 1448-
679   1460 (2012).
680 56 Minami, I. *et al.* A small molecule that promotes cardiac differentiation of human
681   pluripotent stem cells under defined, cytokine-and xeno-free conditions. *Cell reports.* **2**,
682   1448-1460 (2012).
683 57 Isomura, A., Hörning, M., Agladze, K. & Yoshikawa, K. Eliminating spiral waves pinned to an
684   anatomical obstacle in cardiac myocytes by high-frequency stimuli. *Physical Review E.* **78**,
685   066216 (2008).
686 58 Tripathi, S. *et al.* Meta-and orthogonal integration of influenza "OMICs" data defines a role
687   for UBR4 in virus budding. *Cell host & microbe.* **18**, 723-735 (2015).
688
689

690　**Supplementary Information**

691

692　**Circulating traveling waves enhance the maturation of hiPSC-derived**

693　**cardiomyocytes in self-organized tissue rings**

694

695　**Mathematical model**

696　We constructed a mathematical model to simulate the phenomena observed in experiments.

697　This model comprises two critical parts: 1) modeling of the action potential (AP) in a cell and

698　2) coupling between two neighboring cells. First, when we simulated the AP of a single

699　human induced pluripotent stem cell-derived cardiomyocyte (hiPSC-CM), we referenced the

700　classic Priebe & Beuckelmann (PB) model[1] of human ventricular AP based on the Hodgkin–

701　Huxley formalism, with the equations derived from experimental data. To increase

702　computational efficiency and stability, we referenced Panfilov's reformulated model[2] based

703　on the PB model. Unlike human ventricular cells, hiPSC-CMs exhibit an ability to beat

704　spontaneously, indicating that hiPSC-CMs are similar to sinoatrial node cells. Therefore, we

705　added hyperpolarization-activated current[3], I_f, to reformulate the PB model. There was

706　evidence that hiPSC-CMs differed significantly from adult ventricular CMs according to their

707　reduced inward rectifier K^+ currents (I_{K1}) and the presence of prominent pacemaker currents

708　(I_f) that contribute to hiPSC-CM automaticity[4]. Therefore, we changed the maximum

709　conductance value, g_{K1}, of the inward rectifier K^+ currents (I_{K1}) in our mathematical model. A

710　detailed description of the equations governing were described previously[1-3]. Second, there

711　exists a conduction of electrical signals between neighboring cells. Previous studies treated

712　this process using cable equations[5]:

713
$$\frac{\partial V}{\partial t} = \frac{1}{C_m} \frac{a}{2R_i R_{CG}} \frac{\partial^2 V}{\partial x^2} - \frac{1}{C_m} I_{total}$$

(1)

32

714 $$R_i = R_{myo} + \frac{R_g}{\Delta x}$$

715 where V is the membrane potential, C_m is the membrane capacity, I_{total} is the sum of

716 individual membrane ionic currents in a single cell, a is the cell radius, Δx is the length of a

717 single cell, R_{CG} is the ratio between capacitive and geometric areas, and R_i comprises the

718 myoplasmic resistance, R_{myo}, and gap-junction resistance, R_g, as shown. By combining and

719 modifying the above parts, we established a mathematical model of coupled hiPSC-CMs. To

720 create the model in agreement with our experimental results, we set parameters as follows:

721 g_{Na} = 8 nS/pF, g_{to} = 0.35 nS/pF, g_K = 0.1 nS/pF, g_{K1} = 1.17 nS/pF, g_f = 0.08 nS/pF, R_g = 0.1Ω,

722 and R_{myo} = 0.007 Ω/um. We used N cells arranged next to each other in one dimension with

723 periodic boundary conditions to simulate the self-organized tissue ring (SOTR) in the

724 experiment.

725

726 **The dependence of traveling wave (TW) speed on ring diameter**

727 Both in the experiment and the simulation, TW speed increased along with ring diameter (Fig.

728 3d). A key determinant of TW speed was the difference in membrane potential between the

729 yet-to-be-activated cell and the neighboring cell that activates it. All hiPSC-CMs are capable

730 of spontaneously beating, and their APs change periodically. Therefore, maintaining

731 spontaneous beating ability requires the Funny current (hyperpolarization-activated current[3]),

732 I_f, which helps resting cells gradually elevate their APs beyond a threshold, followed by the

733 initiation of depolarization. When stable TWs appear in a ring, the time between two

734 successive beats becomes shorter than that of its own spontaneous beat rate. This is because

735 in the case of TWs, the beating of a cell is due to activation by its neighbor, which would

736 occur prior to its self-activation by the Funny current. The larger the ring diameter, the longer

737 it will take the TW to traverse it, and the longer a cell waits to be activated by its neighbor.

738   This will bring the cell closer to its own self-activation point, resulting in a more rapid

739   activation when the neighbor is activated and a more rapidly propagating TW. The above

740   intuitive argument can be quantitatively expressed in the following equations.

741      $T = n \times Dt$ (2)

742

$$\frac{\partial V}{\partial t} = -\frac{1}{C_m} HH(V) + \frac{1}{C_m} D \frac{\partial^2 V}{\partial x^2}$$

$$\frac{\partial V_i}{\partial t} = -\frac{1}{C_m} HH(V_i) + \frac{1}{C_m} \frac{D}{Dx^2} \{(V_{i+1} - V_i) - (V_i - V_{i-1})\}$$

$$\frac{\partial V_i}{\partial t} = -\frac{1}{C_m} HH(V_i) + \frac{1}{C_m} \frac{D}{Dx^2} \{(V_i(t - Dt) - V_i(t)) - (V_i(t) - V_i(t + Dt))\}$$

$$\frac{\partial V_i}{\partial t} = -\frac{1}{C_m} HH(V_i) + \frac{1}{C_m} \frac{D}{Dx^2} \{(V_i(t - \frac{T}{n}) - V_i(t)) - (V_i(t) - V_i(t + \frac{T}{n}))\}$$

743   (3)

744

745      $V_i(t) = V_i(t + T)$ (4)

746

747   T: the time for one TW to travel around the ring

748   n: the number of cells

749   Δt: the difference in time between the point at which the electrical signal arrives at two

750   adjacent cells

751   V: membrane potential

752   V_i: the membrane potential of the ith cell

753   HH(V): derivation of V and I using the HH equation

754   D: diffusion coefficient

755

756   Given the diameter of the ring, the number of cells is determined (n). Using the

757   periodic boundary condition (Eq. 4), the above equations can be solved to find a relationship

34

758 between the cycle time of the membrane potential of a single cell and the diameter of the ring

759 (Supplementary Fig. 4a).

760 To verify the accuracy of the above explanation, we performed two simulations. First,

761 the Funny current resulted in different AP differences between the two adjacent cells at the

762 wave front in rings with different diameters. Therefore, we deleted the Funny current in every

763 cell, resulting in the loss of spontaneous beating ability and an inability of its AP to change in

764 the resting state over time. This meant that whenever a cell was activated, the difference in

765 AP between the activating cell and the activated cell would be the same, regardless of the

766 diameter of the ring. In this simulation, we found that the diameter of the ring did not affect

767 TW velocity, suggesting that transmitted electrical signals in different ring diameters had no

768 effect on speed due to their shared difference in electrical potential (Supplementary Fig. 4b).

769 Second, we artificially raised the minimum membrane potential of cells in the resting

770 state and maintained their excitable characteristics (with no Funny current). Unlike the first

771 simulation, we established gradients of differences in electrical potential between activating

772 and activated cells. After measuring the propagation velocity of the TWs, we found that the

773 propagation speed decreased as the difference in electrical potential increased
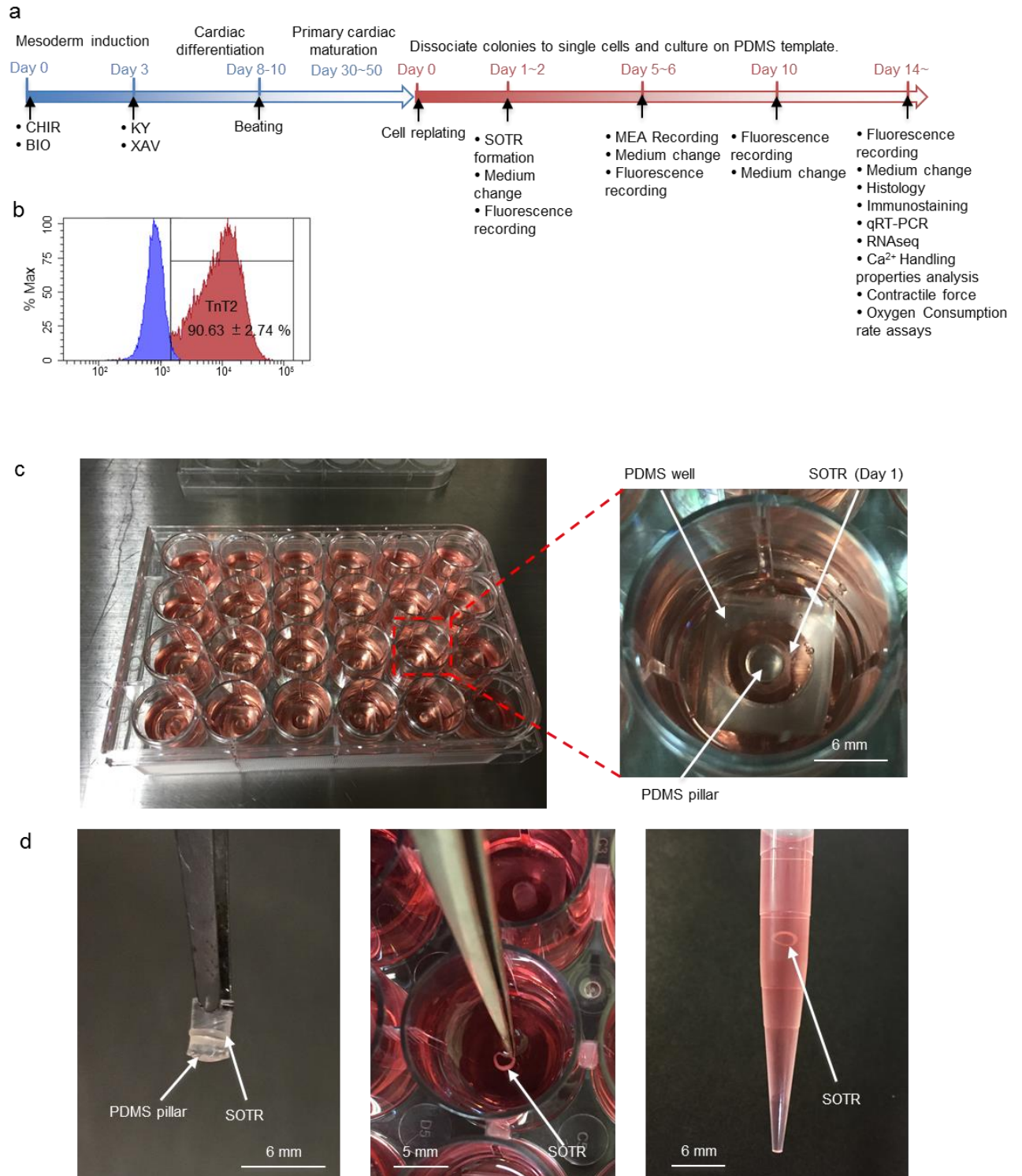
774 (Supplementary Fig. 4c).

775 These two simulations demonstrated that different TW speeds in rings of different

776 diameters were caused by differences in the electrical potential between activated and

777 activating cells. The smaller the ring diameter, the greater the difference in electrical potential

778 and the smaller the propagation speed.

779

780 **Reference**

781 1.   Priebe, L. & Beuckelmann, D. J. Simulation study of cellular electric properties in

782   heart failure. *Circ Res* **82,** 1206–1223 (1998).

35

783   2.   Panfilov, a V. a. of Human Ventricular Cells. **281,** 2296–2308 (2002).

784   3.   Verkerk, A. O., Van Borren, M. M. G. J. & Wilders, R. Calcium transient and sodium-
785   calcium exchange current in human versus rabbit sinoatrial node pacemaker cells. *Sci.*
786   *World J.* **2013,** (2013).

787   4.   Karakikes, I., Ameen, M., Termglinchan, V. & Wu, J. C. Human Induced Pluripotent
788   Stem Cell-Derived Cardiomyocytes: Insights into Molecular, Cellular, and Functional
789   Phenotypes. *Circ. Res.* **117,** 80–88 (2015).

790   5.   Shaw, R. M. & Rudy, Y. Ionic mechanisms of propagation in cardiac tissue. Roles of
791   the sodium and L-type calcium currents during reduced excitability and decreased gap
792   junction coupling. *Circ. Res.* **81,** 727–741 (1997).

Supplementary Figure 1. SOTR formation. (a) Schematic representation of CM differentiation and functional assessment in SOTRs. (b) Flow cytometric analysis of the CMs used for generating SOTRs. (mean ± s.d.; n = 4) (c) SOTRs in a 24-well culture dish. The enlarged figure shows the PDMS well and pillar, between which the cells were plated and

37

798   organized into a tissue ring. (d) SOTR with a PDMS pillar on day 14. The SOTR could be

799   removed from the pillar and transferred with a pipette.

800
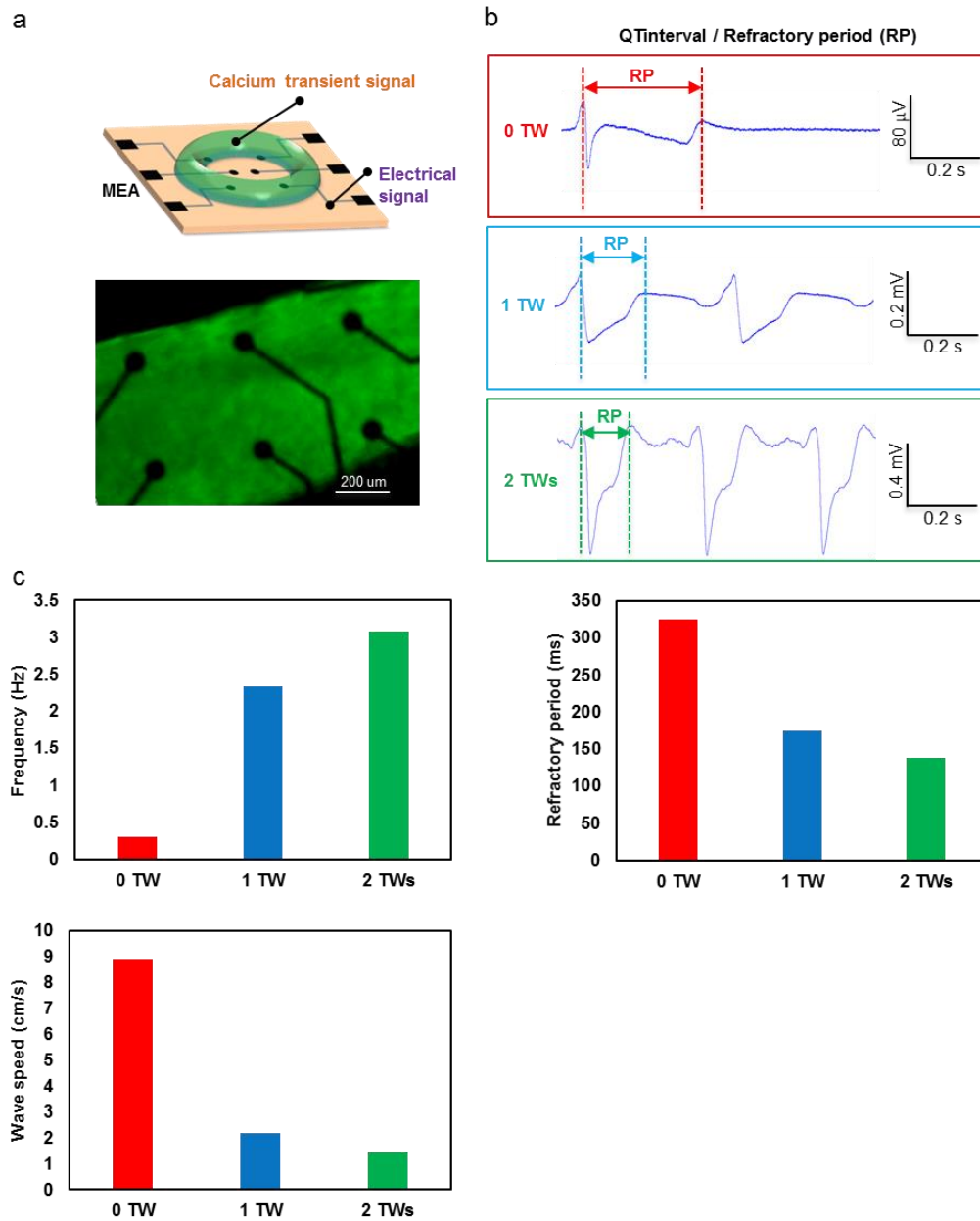
801

802   **Supplementary Figure 2. FP recording by micro-electrode arrays.** (a) Representative

803   setup for FP recording by electrodes underneath a SOTR on day 6. See also supplementary

804   video 5. (b) Representative FP recorded by an electrode underneath a SOTR with or without

805   TWs. (c) Frequency, QT interval (correlated with AP duration and refractory period), and

806   wave speed in SOTRs with or without TWs.

807

808

a

b
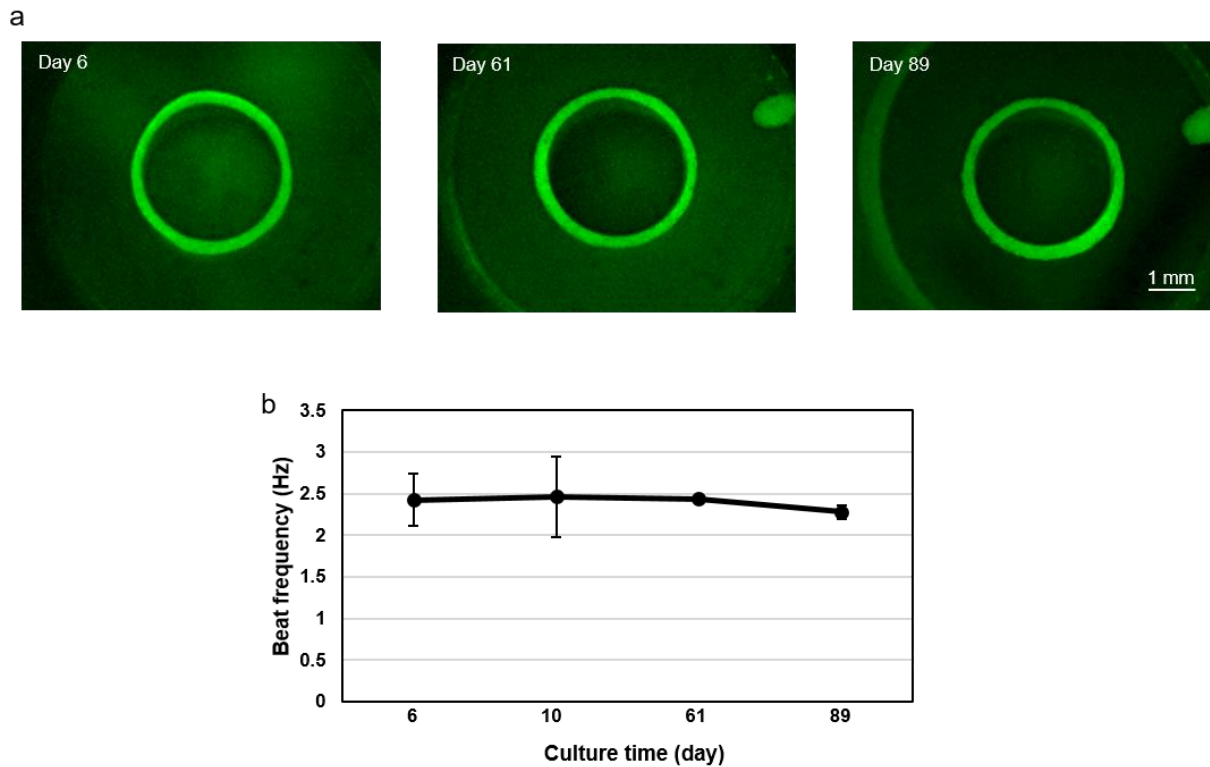
809

810   **Supplementary Figure 3. Maintenance of TWs in SOTRs for >89 days.** (a) Fluorescence

811   images of a SOTR with one TW at different culture times. (b) The beat rate (Hz) of SOTRs

812   with one TW during a long-term culture (mean $\pm$ s.d.; $n = 3$).

813
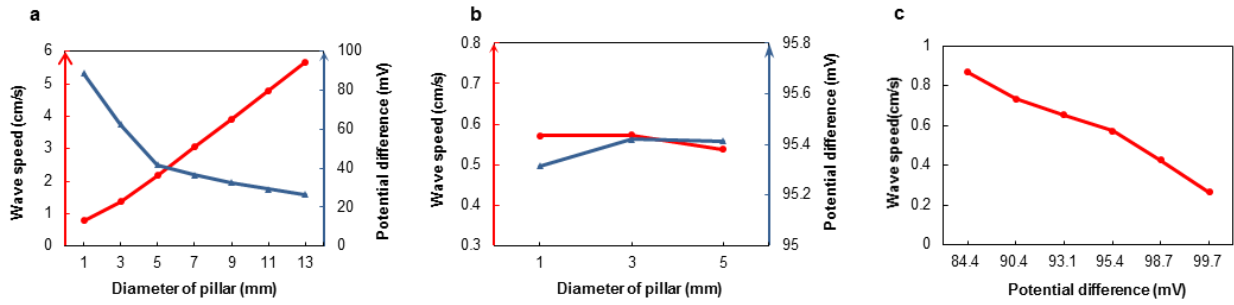
814

815 **Supplementary Figure 4. Relationships between TW speed and differences in**

816 **membrane potential.** (a) Relationships between TW speed, differences in electrical potential

817 between neighboring cells just before activation (at the front tip of the wave), and ring
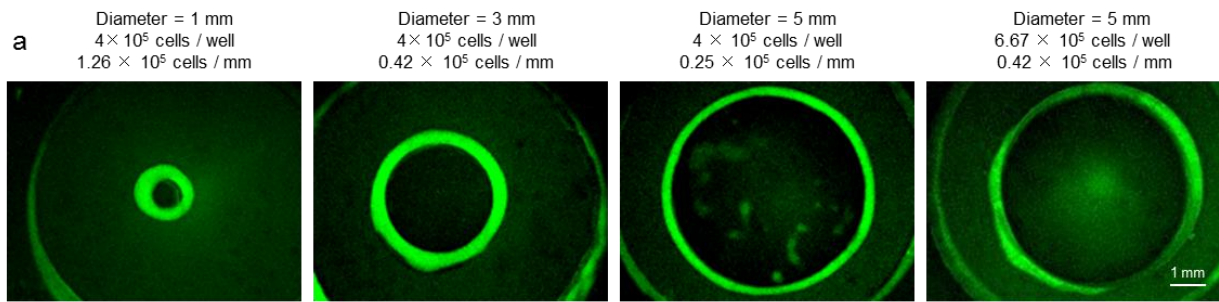
818 diameter. The blue line represents the TW speed, and the orange line represents the difference

819 in electrical potential. (b) The diameter of the ring does not affect TW velocity when cells

820 lose the Funny current. The blue line represents TW velocity, and the orange line represents

821 the difference in electrical potential. (c) Differences in electrical potential affect TW speed.
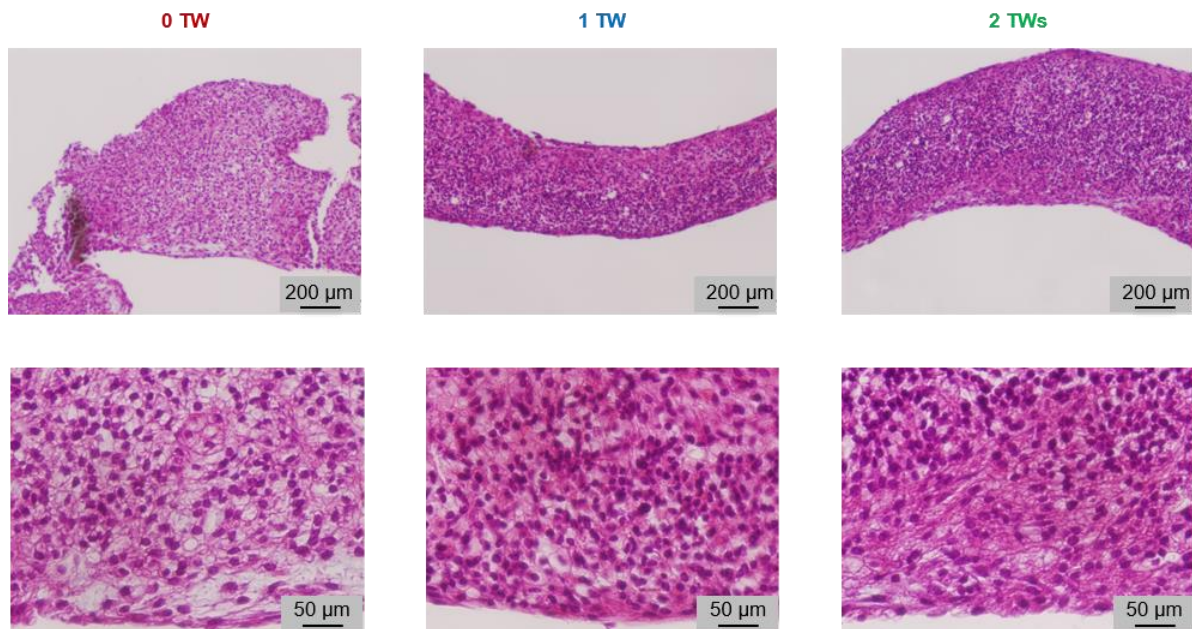
822

Supplementary Figure 5. SOTR formation using pillars with different diameters. (a) Fluorescence images of GCaMP3-positive SOTRs with different diameters at day 6. (b) Percentage of SORTs with TWs on day 6 after cell plating with different pillar diameters.

Supplementary Figure 6. Histology of SOTRs with different TWs on day 6 after cell plating.